Discover Materials

RESEARCH Open Access

Green and ultra-light magnesium foam processed using oyster shell powder as blowing agent

Jonas Isakovic[1*], Hajo Dieringa[1], Daniel Pröfrock[2] and Noomane Ben Khalifa[1,3]

*Correspondence:
Jonas Isakovic
jonas.isakovic@hereon.de
[1]Institute of Material and Process Design, Helmholtz-Zentrum Hereon, Max Planck Str 1, D-21052 Geesthacht, Germany
[2]Institute of Coastal Environmental Chemistry, Helmholtz Zentrum Hereon, Max Planck Str. 1, 21502 Geesthacht, Germany
[3]Institute of Product and Process Innovation, Leuphana University Lüneburg, Universitätsallee 1, 21335 Lüneburg, Germany

Abstract

This study investigates the manufacturing process and material properties of a closed-cell "green" magnesium foam produced by the melt-foaming process using oyster shell powder ($CaCO_3$) as a blowing agent. Oyster shells are a by-product of food and jewellery production, which are considered to be waste and are usually stored in landfills. Alternative uses for the shells are therefore being sought in order to return them to the raw material cycle. A Mg-1Ca alloy is used as the matrix alloy. Magnesium and calcium are elements that are dissolved in seawater and can therefore be extracted from it, for example in desalination plants. We present here the first magnesium foam that has been obtained from magnesium and calcium using oyster shell powder as a blowing agent. This means the foam consists of naturally extractable components, that could also be generated from the Atlantic Ocean or the North Sea, for example. Since the material does not contain any other contamination, e.g. from a technical blowing agent, returning it to marine environment after the end of life by dissolving it in seawater is expected to not cause any ecological or economic damage. Here the production process is described and the dissolution rate in seawater is investigated. The composition and structure of the foam and its mechanical properties are examined. The foam has a fairly homogeneous pore structure, whereby the pore size in the upper area of the foam is slightly increased due to the drainage effect, which also has an effect on the mechanical properties.

Keywords Magnesium foam, Mg-Ca, Oyster shell powder, Ultralightweight, Structural, Circular economy, Net zero, Recycling, Natural products

1 Introduction

The development of light and mechanically strong metallic materials becomes more and more important for transportation industry to reduce energy consumption and CO_2 emissions. In the future, the development of new types of lightweight metallic materials will not be based solely on ores extracted from conventional mines, but the educated consumer will place new demands on material developers regarding sustainability, resource conservation and recyclability. Resource conservation and thinking in closed

cycles (circular economy) will be a purchasing incentive just as important as customer expectations regarding sustainability and fair production with a low CO_2 footprint.

In this environment, natural primary "green" materials or additives are of particular interest, as they typically offer very good traceability to natural biogeochemical cycles. Metallic materials basically have the advantage over polymers and ceramic materials that they can be recycled several times in melt metallurgical processes. In most cases, the recycled metal can be used in an identical way as it was used before recycling. This applies to copper wires, for example, as their electrical conductivity and mechanical properties are the same as those of primary production even in the recycled copper wire [1]. Therefore, a real recycling/circularity is possible in comparison to e.g. most polymeric materials, where often only "downcycling" is possible.

Magnesium-based materials can play out another advantage here. Magnesium can be extracted from natural marine salt water by electrolysis [2]. This has been done for many years at the Dead Sea because of its high Mg^{2+} concentration; Dead Sea Magnesium (DSM) is developing and producing magnesium here [3]. But the extraction of pure magnesium from seawater as a byproduct is also worthwhile, e.g. if drinking water is to be obtained in a desalination plant anyway [4, 5]. During desalination to fresh water, brines which have 3 times the concentration of salts compared to the actual seawater are produced as a waste product [6] and aside magnesium, calcium can also be extracted from these brines. The global desalination capacity of the estimated 15,900 desalination plants sums up to approximately 95 million m^3 per day in 2023 [7]. According to Mayor, the required quantity in 2050 will be up to 170 million m^3 per day [8]. This is an increase of approx. 80%, which reflects the enormous demand for freshwater on the one hand and gives an idea of the quantities of deposited salt on the other. In addition, the European Commission has classified magnesium as one of the 30 "critical raw metals", as this material is of economic importance. To avoid interruption of the supply chain of primary magnesium into the EU, alternative supply and extraction options must be considered in the near future. In particular the recycling of magnesium-based products gains more and more importance since it is listed as critical raw material due to missing diversity in terms of availability of different global producers [9].

Due to the increasing population worldwide, the industrialization of the food sector continues to grow. The worldwide consumption of oysters for food and to produce pearls is behind the problem that oyster shells as a by-product cause a large amount of waste. Due to the low percentage of oyster meat by weight in a farmed oyster, the share of shells is even about 70% [10, 11]. The shells of oysters from aquaculture currently find only few further processing possibilities and are therefore normally deposited as waste, sold or thrown back into the sea to a small extent. The shells are also used as raw material for various applications, such as the production of artificial stones or as an additive for mixing cement [10, 11]. According to FAO figures [12], global oyster production in 2020 and 2021 was about 6.26 and 6.67 million tons by live weight, respectively. This would correspond to a mass of oyster shells of 4.38 and 4.67 million tons, which currently often contaminate coastal regions and freshwater in an uncontrolled manner. Therefore, the use of shells in the production of light metal foams corresponds to a CO_2 net zero and zero cost calculation for the part of the blowing agent and represents a valuable new way to utilize such natural raw materials.

Metal foams are already used in a wide range of applications [13]. These product areas can be divided into structural, functional, and architectural applications. Examples of structural applications are found in lightweight construction using foam-filled profiles and panels [14], but also as energy absorbers for crash structures in the transport sector, e.g. in cars or trains [15]. The areas of application for metal foams as a functional element include sound absorbers [16], heat exchangers due to their good heat transfer properties [17], and as an implant material in the biomedical field, which enables better osseointegration due to its sponge-like structure [18]. In general, metal foams can be produced by various process routes and consist of different materials and alloys. In his review, Singh et al. shows different process methods and the corresponding products that have been developed are available on the market. The materials mostly used are aluminium, iron, copper, nickel, magnesium, and titanium [19]. However, even though many metal foam products are already available on the market, demand is still insufficient. As an example, Hommel et al. mention high costs, lack of design knowledge and missing reference applications for aluminium foam sandwiches. To support the application of such hybrid designs and thus reduce prices, different fields of application are being investigated and motivated. For example, machine components made of aluminium foam sandwich would reduce the mass and improve the behaviour in terms of acceleration and damping effects [20]. Through process parameter-property correlations, missing knowledge about the design properties of metal foams is addressed. How the mechanical properties of metal foams correlate with the pore structure is shown, among many others, by Xia et al. based on a study of the compression properties of closed-cell magnesium foams. Magnesium foams with different porosities and pore sizes (AZ31 alloy) were produced via the melt-foaming process. It is shown in detail that the compressive strength, but also the amount of energy absorption depends on the porosity and the average pore size of the foam [21]. The experiments follow the melt route to produce metal foam. In addition to the direct injection of gas into the melt, a variant of this process involves stirring a powder-bound blowing agent into the melt, which is for aluminium alloys also known as the "ALPORAS"-process. At elevated temperatures, the powder starts to react with the melt and forms bubbles. Solidifying the resulting porous structure creates a foam-like solid body. The final pore structure depends on the reaction of the blowing agent with the melt and finally on the effectively released gas. A higher melting temperature causes a faster reaction, releasing more gas in a shorter time which leads to a higher porosity, a larger pore size and a correspondingly smaller number of pores [22]. If the melt is at low temperature or heated to high temperature, the foaming process will result in either a casting with an undefined pore structure or a defective inhomogeneous porous structure. While titanium hydride (TiH_2) is used for foaming aluminium, calcium carbonate ($CaCO_3$) is mostly used as a blowing agent for magnesium foams. Since magnesium absorbs hydrogen, the use of titanium hydride leads to disadvantages such as rough pore walls in the porous magnesium structures [23]. Yang et al. discusses in detail the decomposition of calcite ($CaCO_3$) in combination with molten magnesium [22]. TGA - DTA analysis shows that the decomposition of $CaCO_3$ corresponds to an endothermic peak temperature of 863 °C. According to Eq. 1, the reaction produces calcium oxide and CO_2. The thermogravimetric analysis of the reaction of untreated $CaCO_3$ mixed with Mg powder shows a mass loss of the sample starting at a temperature of 560 –575 °C (Eq. 2).

According to the results of the differential thermal analysis, the endothermic peak is at 648 °C, which corresponds to the melting temperature of Mg. The chemical reaction (Eq. 2) between blowing agent and liquid magnesium has its exothermic peak at 720 °C [22, 24].

$$CaCO_3\ (s) \rightarrow\ CaO\ (s) + CO_2\ (g) \tag{1}$$

$$Mg + CaCO_3\ (s) \rightarrow\ MgO\ (s) + CaO\ (s) + CO\ (g) \uparrow \tag{2}$$

In the liquid-solid reaction between molten Mg and $CaCO_3$, CO is released in addition to resulting magnesium oxide and calcium oxide [22]. Carbon monoxide gas serves as a blowing agent which forms the pores. CO leaking from the melt reacts completely with the oxygen in the air at 650 °C to CO_2, so that no CO pollution occurs [24].

Use of oyster shells in industrial processes or products where they serve as a source of calcium or calcium carbonate, such as food supplements, cosmetics, medical products, water treatment, soil improvement, or, as in this case, materials synthesis, can be a major contribution to sustainable use of natural resources in the future [10]. A magnesium alloy foam produced using oyster shell powder as a blowing agent has not yet been described in the literature. The use of this natural blowing agent to produce metal foams has so far only been described in the case of aluminium in two previous papers. Thus, in [25], closed-cell foams were prepared from an AlSi7Mg alloy with 1, 3, and 5 wt% oyster shell powder added and stirred during their preparation. It was shown that the addition of 3 wt% oyster shell powder resulted in an optimum porosity, where the pores have a diameter between 1.3 and 3 mm, while the porosity is about 71%. Another paper investigates the influence of different amounts of SiC in a composite foam with an AA7075 matrix and X wt% SiC (X = 0, 3, 6, 9, and 12) as well as 3 wt% TiB_2 [26]. Here, 2.5 wt% oyster shell powder is used as blowing agent and the morphology of the foam and its mechanical properties are investigated. As the SiC content increases, the yield strength and Young's modulus of the hybrid foam composites also increases. The energy absorption also significantly improves with the SiC content and has its maximum at 6 wt%. At higher contents, however, this value drops again.

This paper is a feasibility study on the production of a magnesium foam consisting of a Mg-1Ca alloy foamed with oyster shell powder into a sustainable green material. Magnesium and calcium are components of seawater and can be obtained from e.g. desalination plants, while the oyster shells are a product of the natural growth of oysters. The utilisation of these natural byproducts promotes ecological circularity. Due to its decomposition in seawater, the foam is assumed to be returnable to the ocean at its end of life without generating harmful damage to the general marine environment since it will not contain any other impurities.

2 Materials and methods

2.1 Origin and analysis of oyster shell powder and the used base material

The oyster shell powder was supplied by Trautwein Naturwaren, Karlsruhe, Germany. According to the manufacturer, its composition is: 96 g $CaCO_3$, 0.025 g Mg, 0.05 g K, 0.037 g S, 0.03 g P, 0.1176 g Fe, 0.037 g Mn, 0.0033 g Zn, 0.0009 g Cu, 0.0003 g Mo and 0.0021 g B (per 100 g). Due to its natural origin and an undefined degree of grinding, the characterization of the particle size distribution of the used oyster shell powder has

been carried out with a grid gradation of 125 µm, 90 µm, 75 µm, 63 µm, 45 µm, 32 µm and 20 µm. The powder remaining in the respective sieves is converted into a particle size distribution via the weight difference. The sieving tests were repeated four times. Sieving parameters are 30 min sieving time with 10 s. intervals and a tapping amplitude of 1.5 mm. In addition to the sieve analysis, the oyster shell powder was also examined optically using a Keyence VK-X1050 laser microscope.

Determination of elemental mass fractions in the sample digests was performed using an inductively coupled plasma tandem mass spectrometer (ICP-MS/MS) (Agilent 8800, Agilent Technologies, Tokyo, Japan) coupled to an ESI SC-4 DX FAST autosampler (Elemental Scientific, Omaha, Nebraska, USA) [27]. Experimental details are described in the Appendix 1.

2.2 Melt-foaming process

Figure 1 shows a schematic of the process sequence of the optimized melt foaming method. 250 g of pure magnesium (purity min. 99,9% Mg, manufacturer: HOESCH Metals and Alloys GmbH, Niederzier, Germany) were melted in a 55 mm diameter steel mold. The temperature of the melt was set to 700 °C and checked using a type K thermocouple. As thickening agent 1 wt% calcium (granules, redistilled, -6 mesh, 99.5%, manufacturer: Life Technologies GmbH, Darmstadt, Germany) was added to the melt and stirred for 10 min at 350 rpm. The entire casting process takes place in an inert gas atmosphere of Ar + 2% SF_6. As blowing agent, 2 wt% of milled oyster shell powder was added to the melt. The used powder is as delivered and was heated at 200 °C for 30 min. to remove any moisture. The powder is stirred into the melt with a 3-bladed axial propeller stirrer at 800 rpm. After 10 s of stirring and another 30 s. of holding time, the casting is cooled in water.

2.3 Structural and mechanical analysis

For the characterization of the pore structure, the foamed castings were cut to rectangular samples (30 × 20 × 20 mm) for the analysis of the global pore structure and for the compression tests. X-ray Computed Tomography of the compression test samples were made using a Y.Cougar PRO microfocus X-ray system from yxlon. The reconstructed 3D models were analysed for pore size and cell wall thickness using the Volume Graphics VGStudio MAX software from 2023. For the characterization in terms of determining the density, pore sizes and mechanical properties, we used $n = 8$ samples from the respective areas of each foam. The pore structure analysis in each sample takes place using a threshold value calculation. The CT-scan analysis is performed in a cubic volume

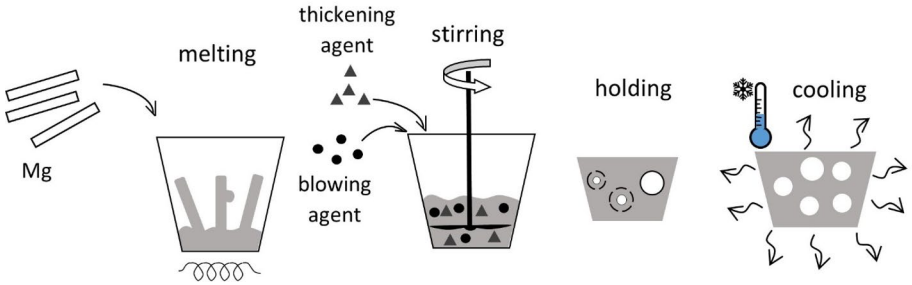

Fig. 1 Schematic of the melt foaming method. After Kucharczyk [23]

with 40 mm edge length corresponding to 1004 voxels in x y z direction. This results in a resolution of 40 µm for all compression samples. The compression tests were carried out using a Zwick Z050 hydraulic universal testing machine at room temperature and a test speed of $1 \times 10^{-2}\ s^{-1}$.

Microstructural characterization was performed using a Zeiss Crossbeam 550 L scanning electron microscope equipped with an energy-dispersive X-ray spectroscopy (EDS) system. The SEM analyses were conducted at an acceleration voltage of 15 kV and a working distance of approximately 15 mm (for EDS, 5 mm). Prior to imaging, the samples were prepared using proven metallographic methods for magnesium sample preparation, like grinding with SiC papers (#800, #2500) and polishing with a hard synthetic fiber cloth and 1 µm diamond suspension. In addition, the samples were further prepared using a Leica EM TIC 3X Ion Beam Milling System for 60 min at an inclination angle of 3°, accelerating voltage of 6 kV, sample rotation of 90° and translation by approx. 10 mm to ensure uniform material remove across the surface.

2.4 Corrosion test

In order to simulate the corrosion behaviour in seawater the magnesium foams were examined using an immersion test in a standard eudiometer set-up. An artificial seawater solution according to ASTM D 1141–90 is used. Its composition is: 24.53 g/l NaCl, 5.2 g/l $MgCl_2$, 4.09 g/l Na_2SO_4, 1.16 g/l $CaCl_2$, 0.695 g/l KCl, 0.201 g/l $NaHCO_3$, 0.101 g/l KBr, 0.027 g/l H_3Bo_3, 0.025 g/l $SrCl_2$, 0.003 g/l NaF. Equation (3) shows the reaction between water and magnesium during corrosion. Gaseous hydrogen is released, which is captured by a measuring column. The samples have a size of $10 \times 10 \times 10$ mm having different densities due to the random pore structure. Each sample is placed in 400 ml of the solution. The solution has a temperature of 22 °C ± 1 °C and is stirred continuously at 100 revolutions per minute. Since the samples have a lower density than water, they were fixed in a net to keep them submerged during the entire experiment. The hydrogen evolution is measured at intervals as an indicator of the corrosion rate. After 10 days (240 h) the corrosion experiments were stopped.

$$Mg + 2H_2O \rightarrow\ Mg\,(OH)_2 + H_2 \uparrow \tag{3}$$

3 Results and discussion

3.1 Composition of Raw materials and chemical analysis

Since the blowing agent in this case is a natural product, the powder does not consist of pure calcium carbonate like a synthetic powder which is produced for the laboratory standard with required quality. Aside $CaCO_3$ oyster shells can contain up to 5% proteins and lipids, which are incorporated during shell growth into the $CaCO_3$ matrix to improve the mechanical shell properties, as well as other trace elements, which reflect the seawater composition during the time of growth. A chemical analysis of the raw materials as well as the final foam material was carried out. The samples were screened for several elements. Table 1 shows the chemical analysis of the magnesium, calcium, and oyster shell powder used, as well as the matrix of the produced foam, for those elements which show mass fractions above the Limit of Detection/ Limit of Quantification (LOD/LOQ) in at least one of the analysed samples. The producer of the oyster material specified mass fractions for some further trace elements. However, due to the small

Table 1 Data compilation of the element analysis of the different Raw materials and the Mg foam (Analysis via ICP-MS/MS, $n = 3$)

	Pure Magnesium		Pure Calcium		Magnesium foam		Oyster shell blowing agent		LOD	LOQ
	Conc. [µg/kg]	U(k = 2)	Conc. [µg/kg]	U(k = 2)	Conc. [µg/kg]	U(k = 2)	Conc. [µg/kg]	U(k = 2)	[µg/kg]	[µg/kg]
Mg	9.9×10^8	7×10^7	< LOD		9.3×10^8	9×10^7	< LOD		30,000	110,000
P	< LOD		< LOD		< LOQ		310,000		7	22
Ca	< LOD		9.1×10^8	7×10^7	1.95×10^7	600,000	4×10^8	4×10^7	9	26
Sc	< LOD		5100	700	< LOQ		2450	240	0.07	0.24
Ge	< LOD		< LOQ		< LOQ		200	700	0.07	0.17
As	< LOD		< LOD		< LOQ		140	250	0.03	0.07
Rb	< LOD		< LOD		< LOD		100	300	0.023	0.05
Sr	150	210	1.26×10^6	70,000	42,000	3000	1.11×10^6	110,000	0.023	0.07
Y	< LOD		270	150	< LOQ		2200	200	0.05	0.17
Ru	< LOD		40	120	< LOD		50	130	0.01	0.025
Pd	< LOD		4500	2600	160	180	3300	800	0.04	0.12
Sb	< LOQ		< LOD		400	800	< LOD		0.13	0.3
Te	< LOQ		200	300	< LOD		100	300	0.017	0.05
Ba	1900	1000	1000	500	1500	600	2800	600	0.5	1.5
Sm	< LOD		< LOD		< LOD		300	210	0.026	0.09
Eu	< LOD		< LOQ		< LOQ		80	50	0.0006	0.0019
Gd	< LOD		< LOD		< LOD		340	140	0.08	0.25
Tb	< LOD		< LOD		< LOD		46	20	0.013	0.04
Dy	< LOD		< LOD		< LOD		340	180	0.1	0.3
Ho	< LOD		< LOD		< LOD		70	30	0.011	0.04
Er	< LOD		< LOD		< LOD		180	100	0.028	0.09
Tm	< LOD		< LOD		< LOD		27	25	0.0024	0.008
Yb	< LOD		10	40	< LOD		200	160	0.00025	0.0007
Lu	< LOD		< LOD		< LOD		20	28	0.0021	0.007

sample mass used for digestion (250 mg) and after the required sample matrix dilution, their concentration was below the LOD/LOQ of the used method.

In the used Mg raw material aside small mass fractions of Sr and Ba no further contaminations above the LOD/LOQ of the used method could be observed. In particular no toxicologically relevant metals have been detected. The oyster material showed aside Ca high mass fractions of Sr and P, which is normal for such natural materials of marine origin. Aside this, the material contains different other trace elements in small mass fractions such as Rb, Ba, different rare earth elements or As, which reflects the average seawater composition at the location were the oysters have been cultivated. Again, no toxicologically relevant metals have been detected, which underlines the potential of such raw materials for the production of new pollution free, easy to recycle metal foam materials. The used Ca material showed only some Sr impurities. All other elements showed only small mass fractions.

In the Mg foam material the high mass fractions of Ca and Sr originating from the used oyster material as well as the used Ca based thickening agent is well visible, while all other impurities show low mass fractions or were below the LOD/LOQ due to the small mass fraction of the raw materials (around 2 wt%) that has been used during foam production. Overall, the comparison of the values of the base material and the values of the samples shows that different element concentrations change as a result of the

process. The final foam material does not show any toxicologically relevant metals or those which could originate from the used melting setup.

An important difference to industrially produced calcium carbonate according to chemical standards, besides the purity of the material, is the difference in size of the particles. The particles cover a size range from 200 µm to less than 1 µm and are characterized by a crystalline structure, see Fig. 2a and b. The particle size distribution diagram in Fig. 2c shows the results of the sieve analyses of the oyster shell powder. The largest proportion (20.5%) of the particles measured are in the fraction between 45 µm and 63 µm. The median particle size is 66 µm. The percentiles D10 and D90 are 28 µm and 125 µm respectively. 1.8% of the powder is smaller than 20 µm and 9.6% of the powder is larger than 125 µm. The result of the particle size analysis shows that the oyster shell powder used has as received only undergone a coarse grinding step. No further processing technique was used to separate the powder into fractions of different particle sizes.

3.2 Process and pore structure analysis

In the foaming process where gas is directly injected into the melt, the pore structure grows randomly. The bubbles created by the blowing agent rise, settle on the surface and form the cellular structure. The properties of the melt determine the resulting packing density, the distribution and the diameter of the pores and therefore the structure of the foam as well as the shape of the cell walls. Figure 3a shows a cross-section of a cast foam block with marked areas (TOP, MID, BOT) from which the rectangular samples (Fig. 3b) were taken for structural analysis and compression testing. The diagram in Fig. 3a shows the density distribution across the height of the foam, revealing a gradient. Due to more material accumulation in the lower part of the foam, the density is higher than in the upper part of the foam, which is more porous. The oyster shell powder was used as received. In the experiments conducted, according to [22], the melt temperature of 700 °C is already 20 °C below the exothermic peak of the reaction of the $CaCO_3$ blowing agent with magnesium. Nevertheless, the experiments have shown that the reaction takes place instantaneously. Stirring ensures that the powder is well distributed and dispersed in the melt immediately.

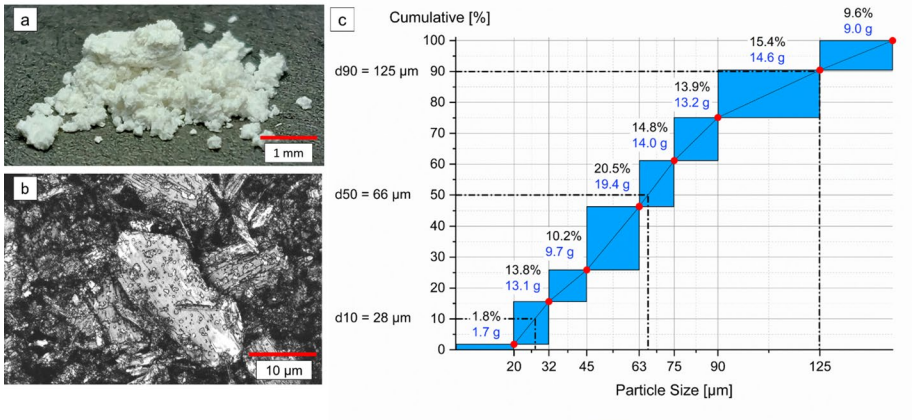

Fig. 2 (**a**) Image of the ground oyster shell as received, (**b**) Close-up of the powder with the laser scanning microscope, (**c**) Particle size distribution diagram of the sieve fractions

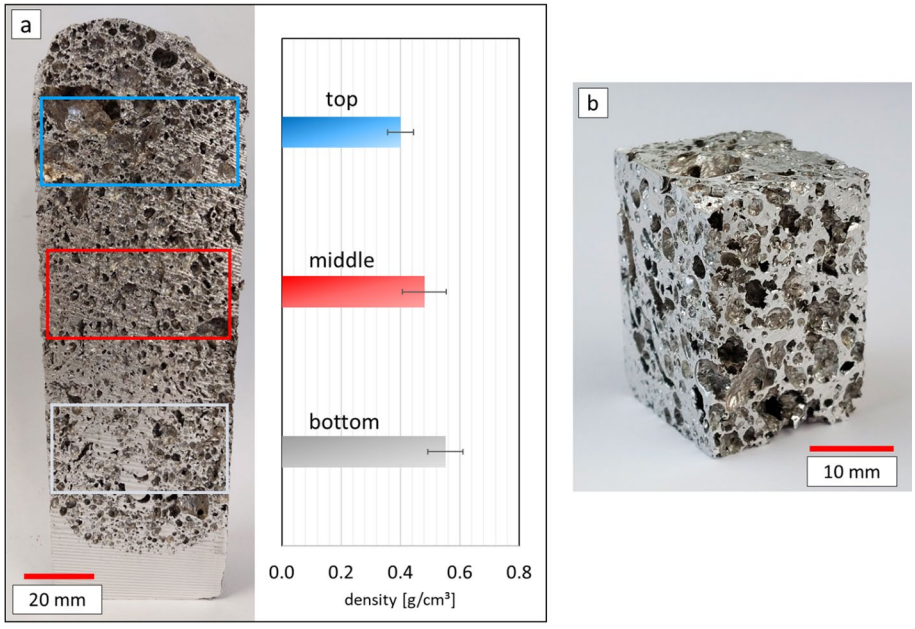

Fig. 3 (**a**) Cross-sectional view of the Mg-1Ca foam (hight: ~190 mm width: ~55 mm) and diagram of density distribution, (**b**) rectangular sample (30 × 20 × 20 mm) for the analysis of the pore structure and compression testing

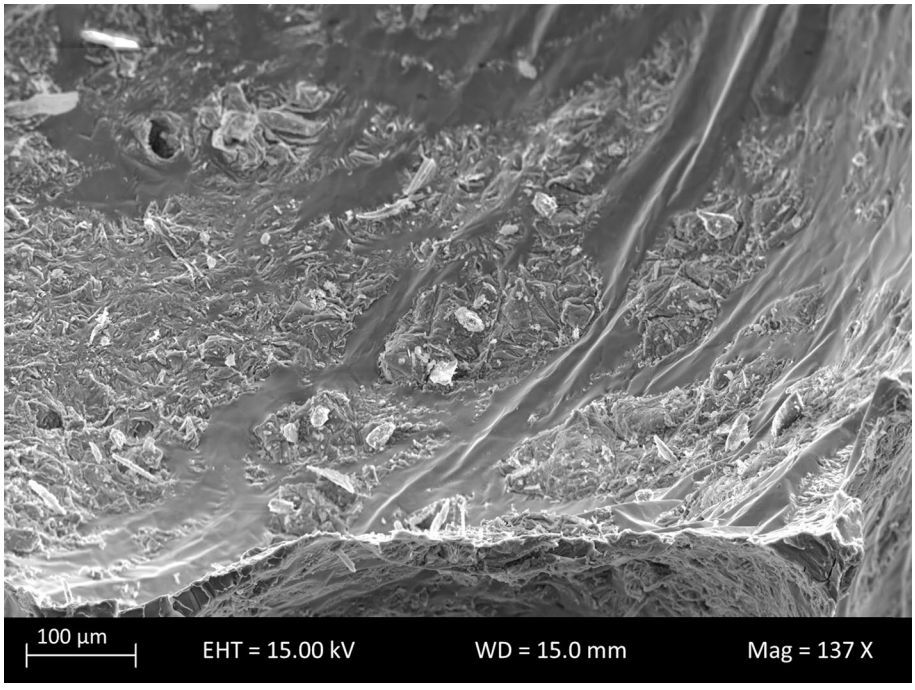

Fig. 4 (**a**) SEM micrograph of a fractured pore in the Mg-1Ca foam, revealing the pore wall morphology and embedded particles

Samples were taken from the foam produced and prepared for examination in a scanning electron microscope. Figure 4 shows the inside of a pore. White particle-like structures can be seen on the cell wall next to blank, clear metallic areas. Point analyses were performed by EDS to investigate the white particles. Figure 5 presents two representative spectra of the measurements on the particles (spectra 1 & 2) together with a

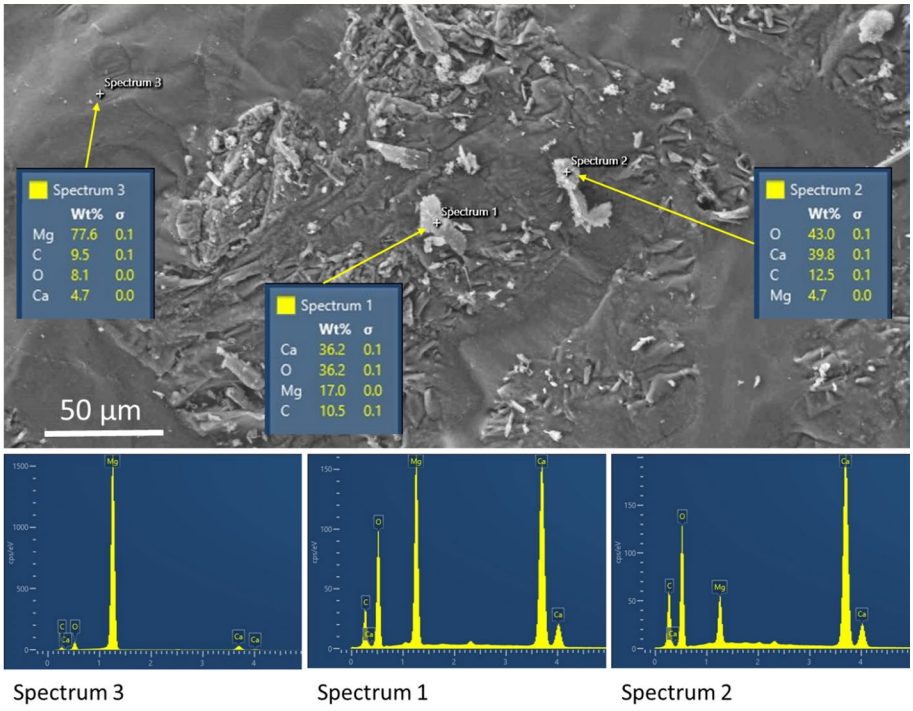

Fig. 5 Local particle accumulation in the pore of the Mg-1Ca foam: Indicated locations of the EDS point analyses, corresponding spectra and quantified elemental composition are shown alongside

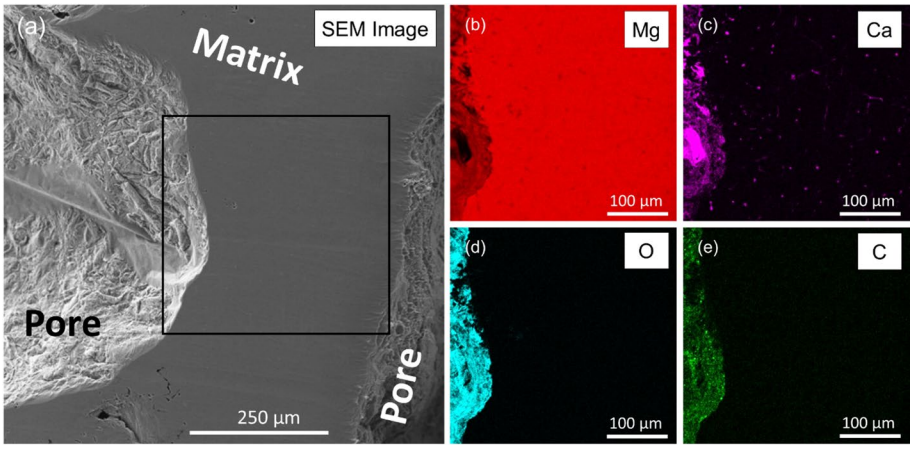

Fig. 6 (**a**) EDS analysis of the Mg-1Ca foam. (**a**) SEM image of the analyzed region; elemental maps showing the distribution of (**b**) Mg, (**c**) Ca, (**d**) O, and (**e**) C

reference spectrum from the surrounding metallic matrix (spectrum 3). Spectra 1 and 2 show pronounced calcium peaks accompanied by oxygen and carbon signals. The determined weight percentages of the elements correspond to the stoichiometric composition of CaCO3. This shows that residual blowing agent is present within the pores, indicating incomplete reaction during the melt foaming process. The formation of gas bubbles during foaming can lead to a local isolation of powder particles from the magnesium melt, interrupting complete reaction.

To evaluate whether particles are present in the metallic matrix, EDS mapping was performed on a representative cell wall, see Fig. 6a. The square section shown in the

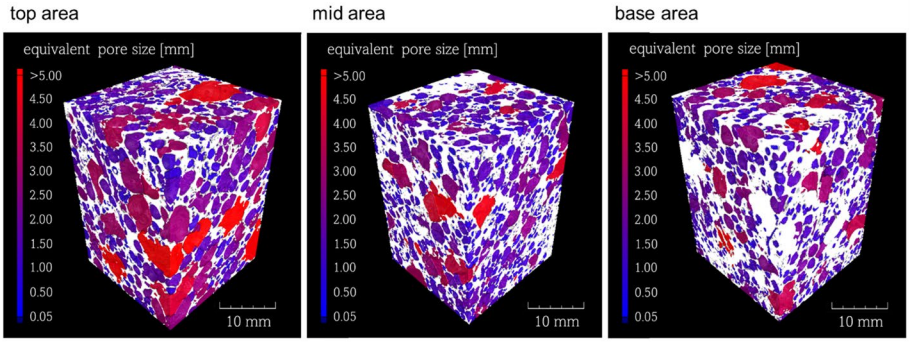

Fig. 7 CT-scan of compression test sample from top, middle and base area of the foamed casting

Table 2 Structural and mechanical properties of the magnesium foams

Area	Density [g/cm³]	Relative density [-]	Eq. av. Pore diameter [mm]	Cell wall thickness [mm]	Compressive strength [MPa]	Relative Yield stress [-]
Top	0.40 ± 0.04	0.23 ± 0.03	1.02 ± 0.70	0.47 ± 0.29	3.27 ± 0.85	0.06 ± 0.02
Mid	0.48 ± 0.07	0.27 ± 0.04	0.93 ± 0.63	0.51 ± 0.39	4.43 ± 1.28	0.08 ± 0.02
Bot	0.55 ± 0.06	0.32 ± 0.03	0.89 ± 0.61	0.66 ± 0.51	6.15 ± 1.13	0.11 ± 0.02

SEM image shows the area in which the element mapping took place. Element maps for magnesium, calcium, oxygen, and carbon are shown, see Fig. 6b – 6e. Small amounts of calcium are present in solid solution in the magnesium matrix as expected in an Mg-1Ca alloy. No residuals of $CaCO_3$ are present in the metallic matrix. In contrast, the oxygen and carbon signals are confined to the pore wall region, suggesting the presence of residual $CaCO_3$ on top auf the surface of the cell wall.

To estimate the maximum amount of CO_2/CO that can be formed, we performed a volumetric calculation based on the amount of oyster shell powder added. By adding 2% by weight of oyster shell powder to 252.5 g of the Mg-1Ca alloy, we added 4.85 g of $CaCO_3$, which corresponds to 4.84×10^{-2} mol. Since one mole of $CaCO_3$ produces one mole of CO_2 or CO, we can estimate the volume of the gas produced using the general gas equation. This is 3920 cm³. The foam produced has a total volume of approximately 700 cm³. After taking into account the porosity of the foam, it can be determined that approximately 510 cm³ of gas is present in the pore structure. This means, on the one hand, that a certain portion of the blowing agent was not converted, as we have shown in SEM investigation already. On the other hand, it was also found that some of the gas escapes into the atmosphere through the surface of the melt during foaming and is therefore lost to the pore structure.

For detailed pore structure analysis, CT-Scans reconstructed with the Volume Graphics software were carried out. Figure 7 shows compression test samples with a representative pore structure of the produced foam from the top, middle and base area of the casting. The pore arrangement, size and cell wall thickness differ. The density of the samples is 0.40 ± 0.04 g/cm³ for the upper part of the foam, 0.48 ± 0.07 g/cm³ for the middle part and 0.55 ± 0.06 g/cm³ for the lower part of the casting, see also Table 2; Fig. 3a. The average density over the full casting is 0.48 ± 0.07 g/cm³. The comparison with the density of pure magnesium with 1.74 g/cm³ shows the extent of the further weight reduction due to the cellular shape of the material.

The pore sizes are further investigated by analysing the equivalent diameter of the pores, which corresponds to the diameter of a sphere with the same volume. The pore size analysis shows an equivalent average pore diameter of 0.95 mm ± 0.65 mm. Figure 8 illustrates the histogram of the pore diameter of the Mg-1Ca foam casting. As the distribution diagram shows, a difference of the equivalent pore diameter can be seen from the upper and middle areas to the lower area of the casting. The number of smaller pores is higher in the lower part of the metal foam. Vice versa, the number of larger pores is higher in the upper part of the metal foam which is in line with the data from the middle section. The equivalent pore diameter in the upper area of the foam is 1.02 ± 0.70 mm, in the middle area it is 0.93 ± 0.63 mm, and in the lower area it is 0.89 ± 0.61 mm, see also Table 2; Fig. 8. The evaluation of the pore size distribution as well as the 3D analysis of the compression test samples shows that occasionally larger pores with a diameter > 5 mm a rather found in the top area. The highest number of pores in both areas of the foam have an equivalent diameter between 0.5 and 0.7 mm.

Important factors for the application and the associated requirements for these lightweight components are generally the density of the foam, the pore size and distribution and the thickness and shape of the cell walls, as these are the main properties alongside the selected material or alloy [22].

The analysis of the cell wall thickness, results in an average value of 0.55 mm ± 0.40 mm. A closer look at the pore structure of the samples from the upper part of the casting and the base part reveals differences. On average, the cell wall thickness of the foam structure in the upper area is 0.47 mm ± 0.29 mm, in the middle area it is 0.51 mm ± 0.39 mm and in the base of the foam it is 0.66 mm ± 0.51 mm, see Table 2. Figure 9a and b illustrate that the thickness of the intact cell walls between pores is in the range of 0.1 –1 mm. Due to the distribution of the pores and their different sizes, individual accumulations of the

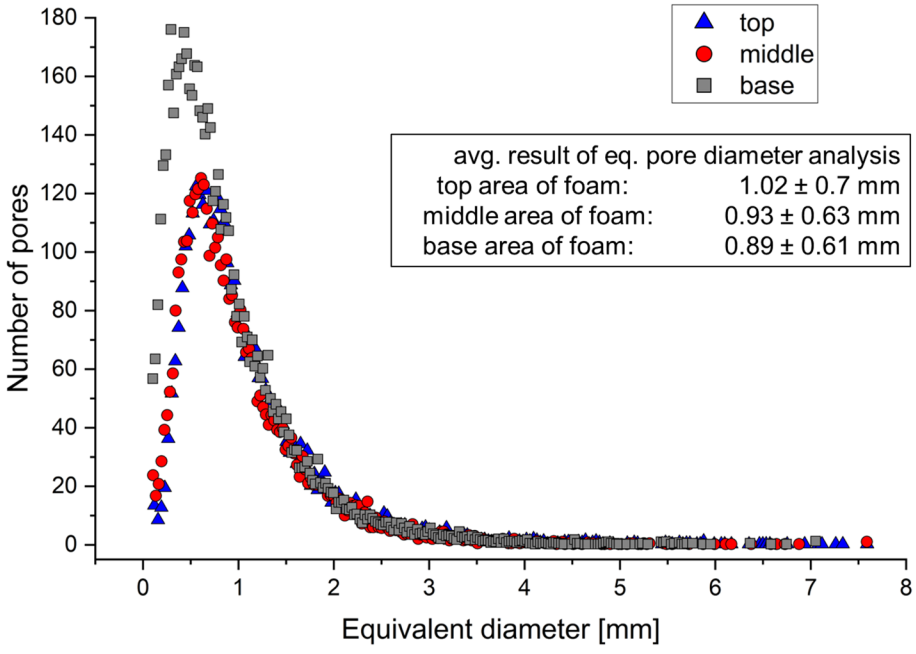

Fig. 8 Histogram of the pore size distribution comparing the top, middle and bottom area of a Mg-1Ca metal foam

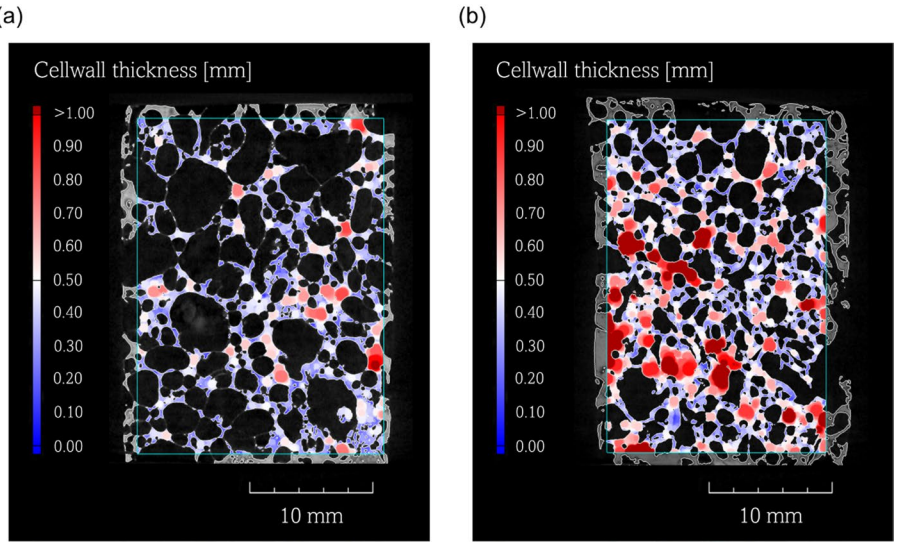

Fig. 9 Cell wall analysis of compression test samples from the upper (**a**) and base (**b**) area of the magnesium foam

alloy can be seen. These areas of the metal matrix have a size of up to 2.5 mm and are visible in the samples from the base of the casting, see Fig. 9b.

The analysis of the pore structure of the magnesium foam shows the influence of the gravity-induced drainage effect. Thinning of the liquid film while foaming can lead to a critical cell wall thickness, resulting in rupture and an inhomogeneous pore structure. A reduced drainage of the melt leads to a more homogeneously distributed pore size in the solidified foam. Since the gas in the melt tends to rise quickly to the surface of the melt and leave the liquid, increasing the viscosity of the melt is a common technique to counteract this [28]. Park et al. show in their work with rheological investigations how temperature changes and the addition of calcium as a thickening agent changes the viscosity of a AZ91 melt after a defined stirring time. The viscosity of AZ91 increases during cooling from approximately 4.3–4.4 mPa·s at 700 °C to approximately 4.8–4.9 mPa·s at 600 °C. The addition of 1.5 wt% Ca further increases the viscosity under stirring (700 rpm, 10 min.) at a constant temperature of 600 °C to approximately 13 mPa·s, demonstrating the thickening effect of calcium [29]. The stabilizing mechanism of solidifying metal foams also involves creating physical barriers in the melt that slow thinning of fluid films and prevents collapse of pores. Adding calcium carbonate ($CaCO_3$) to a magnesium melt as a blowing agent forms calcium oxide (CaO) and magnesium oxide (MgO), see Eq. 2 [22]. Park et al. describe that the formation of solid particles in the melt alters its flow dynamics, decelerates the rupture of cell walls and inhibits cell coarsening to ensure foam stability [30]. Despite the applied stabilization techniques mentioned above, which enable a generally stable foaming process with pronounced expansion, a slight drainage effect is still observed in the Mg-1Ca foam.

3.3 Mechanical properties of Mg foam

Figure 10 show the results of mechanical compression tests. The stress-strain diagrams taken from samples with different densities can be separated into three sections which are characteristic for mechanical behaviour of cellular materials [31], exemplarily shown for the sample with density of 0.37 g/cm^3 (blue line), see Fig. 10a. The elastic

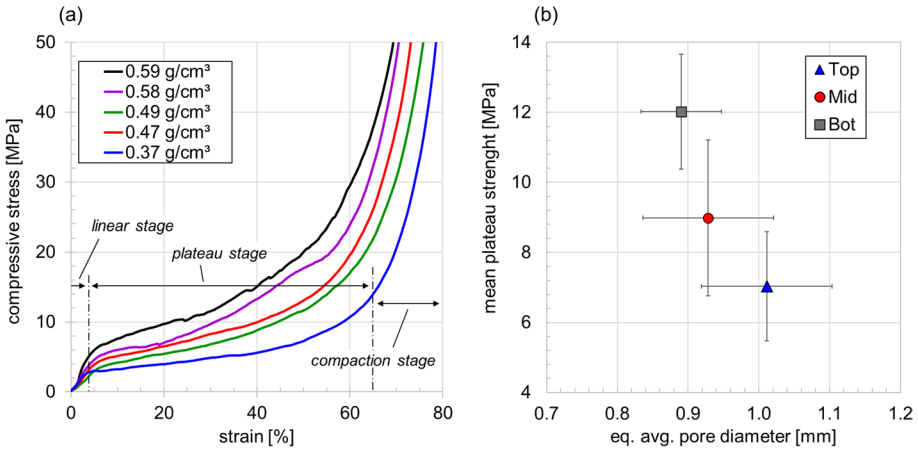

Fig. 10 (**a**) Stress-strain diagram of Mg-1Ca foams of different densities in compression tests, (**b**) Mean plateau strength as a function of the equivalent average pore diameter for pore structures of the investigated areas

deformation of the foam structure takes place in the linear section. After the maximum compressive strength is reached, the first cell walls begin to break under the load. The subsequent plateau phase describes the continuous collapse of the cell structure. In the third or compaction phase, the already broken pore structure is densified, so the stress values increase sharply. While Ashby and Gibson define the onset of densification based on geometric considerations and relative density, the present work determines densification directly from the experimental stress-strain data by identifying the strain at which the local slope of the curve reaches unity [36]. The compressive strength depends on the original density of the samples. The stress-strain diagram shows five samples with densities of 0.37 g/cm³ to 0.59 g/cm³. The sample with a density of 0.37 g/cm³ shows a compressive strength of 3 MPa before entering the plateau phase up to a deformation of about 65%, where densification starts. In comparison, the compressive strength of the foam with a density of 0.59 g/cm³ is 6.8 MPa. Another difference can be seen in the slope of the stress-strain curves in the plateau phase. While the slope of the stress values remains low at a lower density, the slope increases in the samples with a higher density. Compressive strength and relative yield stress in the three regions are given in Table 2. Figure 10b shows the correlation between the mean plateau strength and the equivalent average pore diameter for the investigated areas at the top, middle and bottom. A systematic variation in average plateau strength with pore size is observed. Higher plateau stresses are associated with smaller equivalent pore diameters. Although variations in pore geometry and relative density occur simultaneously and cannot be separated from each other in the available data, the observed trend across the pore structure of the three areas is recognizable within the experimental scatter. The differences in plateau strength can be explained by the resulting structural gradient, with smaller pores and thicker cell walls in the denser areas at the bottom of the foam. The observed variations in plateau strength reflect the combined influence of pore size, local density, and cell wall thickness, which together determine resistance to progressive cell collapse during compression.

Figure 11 shows the comparison of the magnesium foams produced in this work with data of some ALPORAS aluminium foams in the Ashby-Gibson model, which is a commonly accepted method for the prediction of the properties of cellular structures [32–34]. The Ashby-Gibson model relates the relative strength ($\sigma^*/\sigma_{y,\,s}$) (or modulus (E^*/E_s))

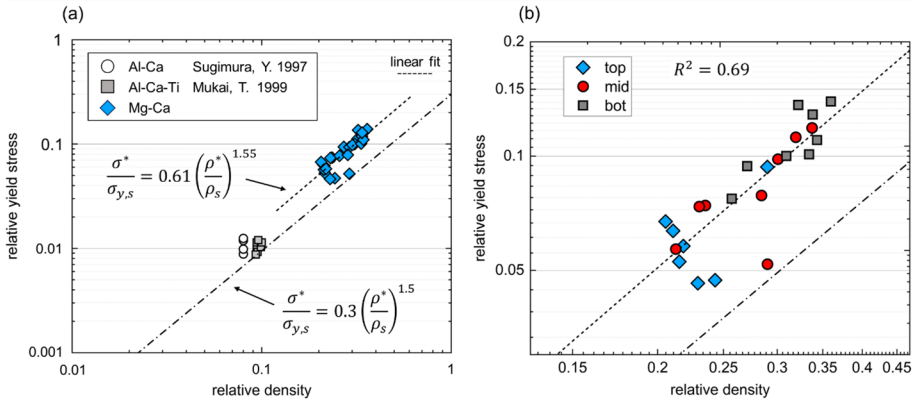

Fig. 11 (**a**) Comparison of Mg-1Ca foams in the Ashby-Gibson model with ALPORAS aluminium foams [32, 33], (**b**) Detailed view of the Ashby-Gibson diagram with region-separated measurement points

of a cellular structure to its relative density (ρ^*/ρ_s), where $\sigma_{y,s}$ is the yield strength of the metal matrix, σ^* is the compressive yield strength of the foam, ρ_s is the density of the matrix metal and ρ^* is the density of the foam, see Eq. 4 [35]. The constant C includes cell shapes and arrangements as well as the intrinsic mechanical properties of the cell wall material. The resulting parameter describes the combined effect of the geometric and material properties and is determined experimentally and numerically. With C = 0.3, generally closed-cell metal foams can be adequately described and compared [35]. According to Ashby, the exponent n in the formula for bend-dominated cellular structures is $n = 1.5$ [36].

$$\frac{\sigma^*}{\sigma_{y,s}} = C\left(\frac{\rho^*}{\rho_s}\right)^n \tag{4}$$

To normalize the yield stress of the Mg-1Ca foam, a solid material compression test with a quasi-static strain rate of 1×10^{-3} s^{-1} at room temperature was carried out. The measurement of the yield stresses of the magnesium samples showed a compressive yield strength of 53.07 MPa ± 2.49 MPa ($n = 10$). Figure 11a shows, the relative density of the magnesium foams is in the range of 0.3, their relative compressive yield strength values are in the range of 0.1. The normalized densities and yield strengths are above those of the ALPORAS aluminium foams. For the data of the Mg-1Ca foams the parameters C and n of the Ashby-Gibson relationship were determined by applying a linear fit, see Fig. 11a. The slope of the fit yields $n = 1.55 \pm 0.22$, which is in very good agreement with the model prediction of $n = 1.5$ by Ashby and Gibson, indicating that the deformation and failure mechanisms of the investigated magnesium foam are consistent with those expected for cellular solids. However, the fitted intercept corresponds to $C = 0.61 \pm 0.18$, which is approximately a factor of two higher than the trend, indicating a systematically higher strength level. In Fig. 11b the data points from bottom, mid and top region of the foam are compared within a detailed Ashby-Gibson plot. The statistical analysis of the linear fit results in a coefficient of determination of $R^2 = 0.69$, which indicates that the fit is suitable for identifying general trends but does not have the precision and robustness required for a predictive model. This rather moderate R^2 value of the linear fit can be attributed to the increased scatter of the data of the upper and middle regions of the foam, while the data points of the lower region show a comparatively good agreement

with the scaling law. The pore structure of the lower region, which has a higher relative density, closely matches the Ashby-Gibson trend and behaves as expected for a cellular solid. In contrast, the measured values for the pore structure in the middle and especially in the upper region show a pronounced spread, indicating varying efficiency in load-bearing capacity, which leads to deviations from the idealized Ashby-Gibson behaviour.

3.4 Dissolving rate in artificial seawater

As all components of the magnesium foam can be extracted from seawater, it should be possible be returned to seawater without harming the environment e.g. at the end of the product's life. In general, the magnesium and calcium ions released into the ocean through dissolution do not lead to a significant increase in overall concentrations, as the volume of seawater is practically infinite. On average, 1 L of seawater contains about 0.42 g of calcium and 1.3 g of magnesium [6], so the additional ions released by dissolution represent only a negligible change compared to the already high background concentrations of these salts. However, the basic pH value of seawater and its general alkalinity would buffer a local increase in pH and the addition of Mg and Ca ions from the dissolution process. This is, of course, only a hypothetical assumption, because for a completely circular use of materials in the future, a separate closed-loop cycle for magnesium alloys is clearly preferable, just as it is for aluminium alloys. To investigate the dissolving rate of the magnesium foams, corrosion tests were carried out in artificial seawater on a laboratory scale. Figure 12 shows the development of hydrogen over time in eudiometer corrosion tests and samples before and after the tests. The graphs in Fig. 12a, representing the hydrogen evolution, have a similar shape for samples with different densities. The reaction rate is high at the beginning and decreases over time. The release of hydrogen corresponds to the shape of a hyperbolic curve, which represents the saturation behaviour of a chemical reaction with depleted reactants. There is no direct correlation between the rate of hydrogen evolution and the density of the foam. Samples #1, #2 and #4 have

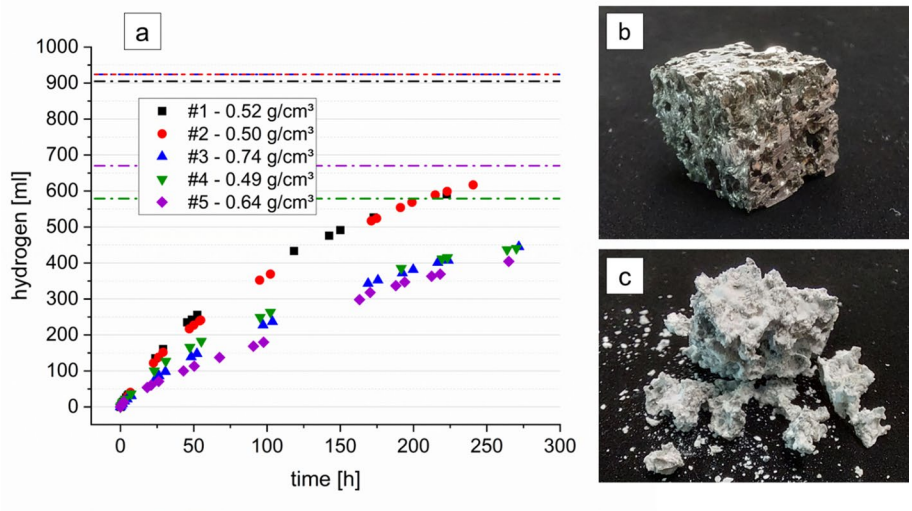

Fig. 12 (**a**) Diagram of hydrogen formation in the eudiometer corrosion tests over time. Mg-1Ca metal foam sample (**b**) before and (**c**) after the corrosion test in artificial seawater for 240 h

approximately the same density of ~ 0.5 g/cm³, but there is a significant difference in the rate of hydrogen formation, see Fig. 12a. Sample #4 shows the same level of hydrogen formation as sample #3 although it has a density of 0.74 g/cm³. The mass of the five samples #1 to #5 (1 g, 1.02 g, 1.02 g, 0.64 g, 0.74 g) can be used to calculate the volume of hydrogen generated according to Eq. 3, assuming that the samples contain 1.8 wt% calcium and thus 98.2 wt% magnesium after the reaction with the oyster shell powder. This is approximately 905 ml for sample #1, 924 ml for each of samples #2 and #3, 579 ml for sample #4 and 670 ml of hydrogen for sample #5. These values thus form the asymptote that the curves tend to reach in the case of full dissolution. The dashed lines in Fig. 12a indicate the maximum amount of hydrogen to be formed after complete dissolution of the sample.

One explanation for the different hydrogen formation rates is that the porosity of the Mg-1Ca foam is higher at lower densities. This results in a larger material surface due to larger pores and thinner cell walls on which reactions can take place. In addition to the corrosion on the surface of the foam, a closed cell foam has internal pores that can still be completely sealed from the electrolyte, which means only the outer surface of the foam is affected. As the corrosion process progresses, the cell walls open and the electrolyte can enter inner pores. This ultimately leads to an extending pore network, as the connections between the pores continue to expand. Under these circumstances the reaction rate can still be lower, even with a low-density sample.

Figure 12b and c show an example of a test sample before and after corrosion test. After ~ 240 h in the artificial seawater, it is evident that the foam cube has been fragmented. Corrosion products are visible on the surface and within the pores of the foam. As observed in the corrosion experiments by Xia and Asadi, the reaction between the artificial seawater environment and magnesium foam primarily results in the formation of hydroxides, along with oxides, which grow as a white layer on the material. This resulting layer is considered a quasi-inactive layer that slows down hydrogen formation. However, it cannot act as corrosion protection, as the presence of chloride ions disrupts this layer, allowing corrosion to continue, see Eq. 5 [37, 38].

$$Mg\,(OH)_2 + 2Cl^- \rightarrow \quad MgCl_2 + 2\,(OH)^- \tag{5}$$

4 Conclusion

In the scope of this work a Mg-1Ca metal foam was produced using the melt foaming method. Natural oyster shell powder, which consists mainly of $CaCO_3$, is used as a blowing agent.

The following conclusion can be drawn from the experiments:

- Mg-1Ca foams have been successfully produced using the melt-foaming process. For the first time, this paper reports on the use of oyster shell powder as a blowing agent for the synthesis of a magnesium foam.
- Since only magnesium, calcium and the oyster shell powder were used and no contamination with other compounds is detectable, the foam is assumed to be returnable to the seawater after the end-of-life without ecological damage.
- The foam has a fairly homogeneous pore structure, whereby the pores in the upper area of the foam are slightly larger than in the lower area. The mechanical properties of the foam depend on its density.

- An Ashby-Gibson plot of the normalized yield strength versus the normalized density shows that this foam corresponds to the expected structure-strength correlation for cellular metallic materials, similar to ALPORAS aluminium foams.
- Foam samples exposed to a corrosive environment in artificial seawater dissolve rapidly to form H_2. After 240 h, the foam samples are fragmented. The corrosion rate does not depend directly on the density of the foam. Pore network and inner surface of the pore structure macroscopically generate a randomized corrosion process.

5 Appendix 1: detailed description of materials analysis

Different cell gas modes have been used to minimize interferences influencing the accurate quantification of the analysed trace metals and metalloids. All preparatory laboratory work was performed in a class 10,000 or class 1000 clean rooms inside a class 100 clean bench. Type I reagent-grade water (18.2 MΩ cm) was obtained from a Milli-Q Integral water purification system equipped with a Q-pod-Element polishing system (Merck-Millipore, Darmstadt, Germany). Analytical grade HNO_3 (w = 65%, Fisher Scientific GmbH) and analytical grade HCl (w = 30%, Carl Roth GmbH + Co. KG, Karlsruhe, Germany) were further purified by double sub-boiling either in perfluoralkoxy-polymer (PFA)-subboling stills (DST-4000 & DST-1000, Savillex, Minnesota, USA) or in a cascade of two quartz stills (AHF Analysentechnik, Tübingen, Germany). The purified acids were stored in cleaned PFA bottles. For sample digestion 250 ± 5 mg of the different analysed materials was filled into pre-cleaned digestion vessels. All sample digests were prepared in triplicates (n = 3). External calibration standard solutions for quantification (all traceable to NIST standards) were prepared from custom-made multi-element standards of different composition (Inorganic Ventures, Christiansburg, USA). Single-element ICP standards (1 g L^{-1}) of Al, In, Nb, Tl, Ti, W were obtained from Merck Millipore. All plastic (LDPE and PP) consumables were pre-cleaned by established protocols in solutions of HNO_3 (w = 1–2%) for a minimum of one week. Before usage the material was rinsed with MilliQ water and dried inside a class 100 clean bench inside a clean room. Multi-element data were processed using MassHunter version 4.4 or higher (Agilent Technologies, Tokyo, Japan) and a custom written Excel© spreadsheet. The isobaric interference of ^{115}Sn on ^{115}In was corrected by peak stripping as implemented in MassHunter using the signal of ^{118}Sn and the isotopic abundances [39]. Procedural LODs (Limits of detection) and LOQs (Limits of quantification) were calculated in accordance with the blank value method described in DIN 32645:2008-11 (DIN e.V. (ed.), 2008) from procedural filtration blanks (n > 3 per campaign). The significant number of digits of concentrations are given according to GUM and EURACHEM guidelines, whereby the uncertainty determines the significant number of digits to be presented with the value [40]. A list of measured isotopes and their detection modes can be found in Table 3. A detailed description of all ICP-MS/MS operating parameters and used cell gas modes can be found also in Table 4. The instrument was tuned daily using a tune solution containing Li, Co Y, Ce and Tl at a concentration of 10 µg L^{-1}. Quantification was performed by external calibration covering a concentration range from 0 µg L^{-1} to 10,000 µg L^{-1} for Mg, Al, K, Ca, Ti, Fe, Mn, Ba and P and 0 µg L^{-1} to 100 µg L^{-1} for all other analytes. Solutions and blanks were prepared on a daily basis from custom made multi-element standards (Inorganic Ventures, Christiansburg, USA). Wash blanks were measured after each sample triplicate to monitor and avoid potential carry-over effects.

Table 3 Instrument settings and operating conditions of the agilent 8800 ICP-MS/MS

Instrument parameters	Operating settings and conditions
Sample introduction	Double-pass spray chamber
Nebulizer	Self-aspirating MicroFlow (ESI)
Interface cones	Nickel
RF power (W)	1550
Carrier gas flow (L min^{-1})	1.07
Make-up gas flow (L min^{-1})	0.1
Used cell gases	He, N_2O
Extract 1 (V)	0
Extract 2 (V)	-175
Omega Bias (V)	-100
Omega Lens (V)	9.6
Q1 Entrance (V)	H_2: 1 He: -1; N_2O: 1
Q1 Exit (V)	H_2: -2 He: -9; N_2O: -2
Cell Focus (V)	H_2: 1 He: 2; N_2O: 7
Cell Entrance (V)	H_2: -50 He: -50; N_2O: -40
Cell Exit (V)	H_2: -60 He: -60; N_2O: -51
Deflect (V)	H_2: -3.4 He: -4.8; N_2O: 8.8
Plate Bias (V)	H_2: -60 He: -60; N_2O: -50
Cell gas flow (mL min^{-1})	H_2: 6.0 He: 4.5; N_2O: 20%
Octpole Bias (V)	H_2: -18 He: -20; N_2O: 0.5
Octpole RF (V)	H_2: 170 He: 200; N_2O: 170
Energy Discrimination (V)	H_2: 0 He: 5; N_2O: -5

Table 4 ICP-MS/MS measured mass-to-charge ratios and gas modes adopted for multi-elemental analysis in this study

Element	m/z (Q1)	m/z (Q2)	cell mode
Mg	24	24	H_2
Al	27	27	H_2
P	31	47	N_2O
Ca	40	40	H_2
Sc	45	61	N_2O
Zn	66		He
Ga	71		He
Ge	72	88	N_2O
As	75	91	N_2O
Rb	85		He
Sr	88		He
Y	89	105	N_2O
Nb	93	125	N_2O
Ru	101		He
Pd	105		He
Cd	111		He
In	115	115	N_2O
Sb	121		He
Te	125	125	N_2O
Ba	137	153	N_2O
La	139	155	N_2O
Ce	140	156	N_2O
Pr	141	157	N_2O
Nd	146	162	N_2O
Sm	147	163	N_2O
Eu	153	169	N_2O
Gd	157	173	N_2O
Tb	159	175	N_2O
Dy	163	179	N_2O
Ho	165	181	N_2O
Er	166	182	N_2O
Tm	169	185	N_2O
Yb	172	188	N_2O
Lu	175	191	N_2O
Ta	181	213	N_2O

Acknowledgements
We thank Jose Victoria Hernandez, Juan-Jose Trujillo-Tadeo, and Falk Dorn for their assistance and guidance in the SEM/EDS characterization process.

Author contributions
Jonas Isakovic: Validation, Formal analysis, Investigation, Writing – original draft, Visualization. Hajo Dieringa: Conceptualization, Methodology, Writing – review & editing, Funding acquisition. Daniel Pröfrock: Investigation, Writing – review & editing. Noomane Ben Khalifa: Resources, Supervision, Funding acquisition.

Funding
Open Access funding enabled and organized by Projekt DEAL. The research was funded by the German Federal Ministry of Education and Research as part of the project "TrICo - Transformation through Innovation and Cooperation in Communities, sub-project: Community Sustainable Production" funding code: 03IHS284B.

Data availability
The authors declare that the data supporting the findings of this study are available within the paper and its Supplementary Information files. Should any raw data files be needed in another format they are available from the corresponding author upon reasonable request.

Declarations

Ethics approval and consent to participate
Not required for this work.

Consent for publication
Not required for this work.

Competing interests
The authors declare no competing interests.

Clinical trial
Not required for this work.

Received: 17 September 2025 / Accepted: 6 February 2026
Published online: 08 March 2026

References

1. Villalba G, Segarra M, Fernandez AI, Chimenos JM, Espiell F. A proposal for quantifying the recyclability of materials, resources, resources. Conserv Recycling. 2002;37(1):39–53. https://doi.org/10.1016/S0921-3449(02)00056-3.
2. Zahedi MM, Ghasemi SM. Separation study of Mg^{+2} from seawater and RO Brine through a facilitated bulk liquid membrane transport using 18-Crown-6. J Water Reuse Desalin. 2017;7(4):468–75. https://doi.org/10.2166/wrd.2016.103.
3. Bronfin B, Moscovitch N, Trostenetsky V, Gerzberg G, Nagar N, Yehuda R. High Performance HPDC Alloys as Replacements for A380 Aluminum Alloy. Magnesium Technology (2008), Eds: Pekguleryuz MO, Neelameggham NR, Beals RS, and Nyberg EA (TMS) 2008;411–415.
4. Cipollina A, Misseri A, D'Alì Staiti G, Galia A, Micale G, Scialdone O. Integrated production of fresh water, sea salt and magnesium from sea water. Desalin Water Treat. 2012;49(1):390–403. https://doi.org/10.1080/19443994.2012.699340.
5. Wang Q, Nakouzi E, Ryan EA, Subban CV. Flow-Assisted selective mineral extraction from seawater. Environ Sci Technol Lett. 2022;9:645–9. https://doi.org/10.1021/acs.estlett.2c00229.
6. Fontana D, Forte F, Pietrantonio M, Pucciarmati S, Marcoaldi C. Magnesium recovery from seawater desalination brines: a technical review. Environ Dev Sustain. 2023;25(12):13733–54. https://doi.org/10.1007/s10668-022-02663-2.
7. Jones E, Qadir M, van Vliet MTH, Smakhtin V, Kang SM. The state of desalination and Brine production: A global outlook: sci. Total Environ. 2019;657:1343–56. https://doi.org/10.1016/j.scitotenv.2018.12.076.
8. Mayor B. Growth patterns in mature desalination technologies and analogies with the energy field. Desalination. 2019;457:75–84. https://doi.org/10.1016/j.desal.2019.01.029.
9. COM(2020)474, Final communication from the Commission to the European Parliament, the Council, the European Economic and Social Committee and the Committee of the Regions. In Critical raw materials resilience: Charting a path towards greater security and sustainability. (2020).
10. Bonnard M, Boury B, Parrot I. Key insight, Tools, and future prospects on oyster shell end-of-life: A critical analysis of sustainable solutions. Environ Sci Technol. 2020;54:26–38. https://doi.org/10.1021/acs.est.9b03736.
11. Silva TH, Mesquita-Guimaraes J, Henriques B, Silva FS, Fredel MC. The potential use of oyster shell waste in new value-added by-products. Resources. 2019;8:13. https://doi.org/10.3390/resources8010013.
12. FAO, Global Production. Fisheries and Aquaculture Division. Rome. https://www.fao.org/fishery/en/collection/global_production?lang=en (accessed 11 May 2023).
13. García-Moreno F. Commercial applications of metal foams: their properties and production. Materials. 2016;9:85. https://doi.org/10.3390/ma9020085.
14. Banhart J. Seeliger. Aluminium foam sandwich panels: Manufacture, metallurgy and applications. Adv Engin Mater. 2008;10(9):793–802. https://doi.org/10.1002/adem.200800091.
15. Zarei HR, Kröger M. Bending behavior of empty and foam-filled beams: structural optimization. Int J Impact Eng. 2008;35(6):521–9. https://doi.org/10.1016/j.ijimpeng.2007.05.003.
16. Lu TJ, Hess A, Ashby MF. Sound absorption in metallic foams. J Appl Phys. 1999;85(11):7528–39. https://doi.org/10.1063/1.370550.
17. Hassan AM, Alwan AA, Hamzah HK. Metallic foam with cross flow heat exchanger: A review of parameters, performance, and challenges. Heat Transf. 2023;52(3):2618–50. https://doi.org/10.1002/htj.22798.
18. Murr LE. Strategies for creating living, additively manufactured, open-cellular metal and alloy implants by promoting osseointegration, osteoinduction and vascularization: an overview. J Mater Sci Technol. 2019;35(2):231–41. https://doi.org/10.1016/j.jmst.2018.09.003.
19. Singh S, Bhatnagar N. A survey of fabrication and application of metallic foams (1925–2017). J Porous Mater. 2018;25(2):537–54. https://doi.org/10.1007/s10934-017-0467-1.
20. Hommel P, Roth D, Binz H. Derivation of motivators for the use of aluminum foam sandwich and advantageous applications. Proc Des Soc. 2021;1:933–42. https://doi.org/10.1017/pds.2021.93.
21. Xia XC, Chen XW, Zhang Z, Chen X, Zhao WM, Liao B, Hur B. Effects of porosity and pore size on the compressive properties of closed-cell Mg alloy foam. J Magnes Alloy. 2013;1(4):330–5. https://doi.org/10.1016/j.jma.2013.11.006.
22. Yang DH, Hur BY, Yang SR. Study on fabrication and foaming mechanism of Mg foam using CaCO3 as blowing agent. J Alloys Compd. 2008;461(1–2):221–7. https://doi.org/10.1016/j.jallcom.2007.07.098.
23. Kucharczyk A, Naplocha K, Kaczmar JW, Dieringa H, Kainer KU. Current status and recent developments in porous magnesium fabrication. Adv Eng Mater. 2017;20:1700562. https://doi.org/10.1002/adem.201700562.
24. Lu Gq, Hao H, Wang F. Preparation of closed-cell Mg foams using SiO2-coated CaCO3 as blowing agent in atmosphere. Trans Nonferrous Met Soc China. 2013;23(6):1832–7. https://doi.org/10.1016/S1003-6326(13)62667-9.
25. Li JW, Shan CF, Teng YL, Gai ZC. Development of low cost lightweight aluminum foam for railway transportation. IOP Conf Series: Mater Sci Eng. 2019;649:012002. https://doi.org/10.1088/1757-899X/649/1/012002.

26. Singh NK, Sethuraman B. Development and characterization of aluminium AA7075 hybrid composite foams (AHCFS) using SiC and TiB_2 reinforcement. Inter Metalcast. 2023;18:212–27. https://doi.org/10.1007/s40962-023-01009-6.
27. Pröfrock D, Prange A. Inductively coupled Plasma–Mass spectrometry (ICP-MS) for quantitative analysis in environmental and life sciences: A review of Challenges, Solutions, and trends. Appl Spectrosc. 2012;66(8):843–68. https://doi.org/10.1366/12-06681.
28. Banhart J. Manufacture, characterization and application of cellular metals and metal foams. Prog Mater Sci. 2001;46:559–632. https://doi.org/10.1016/S0079-6425(00)00002-5.
29. Park SH, Song KH, Um YS, Hur BY. Rheological characteristics of Mg-Al alloys with ceramic particles for meta foam. Mater Sci Forum. 2006;510–511:742–5. https://doi.org/10.4028/www.scientific.net/MSF.510-511.742.
30. Park SH, Seong HG, Song YH, Hur BY. Rheological characteristics of molten metal for casting design. Trans Mat Res Soc Japan. 2007;32:847–50. https://doi.org/10.14723/tmrsj.32.847.
31. Ashby MF, Medalist RFM. The mechanical properties of cellular solids. Metall Trans. 1983;A14:1755–69. https://doi.org/10.1007/BF02645546.
32. Sugimura Y, Meyer J, He MY, Bart-Smith H, Grenstedt J, Evans AG. On the mechanical performance of closed cell al alloy foams. Acta Mater. 1997;45(12):5245–59. https://doi.org/10.1016/S1359-6454(97)00148-1.
33. Mukai T, Kanahashi H, Miyoshi T, Mabuchi M, Nieh TG, Higashi K. Experimental study of energy absorption in a close-celled aluminum foam under dynamic loading. Scr Mater. 1999;40(8):921–7. https://doi.org/10.1016/S1359-6462(99)00038-X.
34. Gibson LJ. Mechanical behaviour of metallic foams. Annu Rev Mater Sci. 2000. https://doi.org/10.1146/annurev.matsci.30.1.191. 30.
35. Gibson LJ, Ashby MF. Cellular Solids: Structure and Properties. 2nd Edition, Cambridge University Press, Cambridge. 1997. https://doi.org/10.1017/CBO9781139878326
36. Ashby MF. The properties of foams and lattices. Philos Trans Math Phys Eng Sci. 2006;364(1838):15–30. https://doi.org/10.1098/rsta.2005.1678.
37. Xia X, Chen X, Zhao W, Xue H, Liao B, Hur B, Wang Z. Corrosion behavior of closed-cell AZ31 Mg alloy foam in NaCl aqueous solutions. Corros Sci. 2014;80:247–56. https://doi.org/10.1016/j.corsci.2013.11.033.
38. Asadi J, Korojy B, Hosseini SA, Alishahi M. Effect of cell structure on mechanical and bio-corrosion behavior of biodegradable Mg-Zn-Ca foam. Mater Today Commun. 2021;28:102715. https://doi.org/10.1016/j.mtcomm.2021.102715.
39. de Laeter JR, Böhlke JK, De Bièvre P, Hidaka H, Peiser HS, Rosman KJR, Taylor PDP. Atomic weights of the elements. Review 2000 (IUPAC Technical Report). Pure Appl. Chem. 2003;75(6):683–800. https://doi.org/10.1351/pac200375060683
40. Ellison SLR, Williams A, editors. Eurachem/CITAC guide: Quantifying Uncertainty in Analytical Measurement. Third edition, (2012) ISBN 978-0-948926-30-3. Available from www.eurachem.org.

Publisher's note